

Realistic and Fast Modeling of Spatial Extremes over Large Geographical Domains

Arnab Hazra¹, Raphaël Huser¹, and David Bolin¹

December 21, 2021

Abstract

Various natural phenomena, such as precipitation, generally exhibit spatial extremal dependence at short distances only, while the dependence usually fades away as the distance between sites increases arbitrarily. However, the available models proposed in the literature for spatial extremes, which are based on max-stable or Pareto processes or comparatively less computationally demanding “sub-asymptotic” models based on Gaussian location and/or scale mixtures, generally assume that spatial extremal dependence persists across the entire spatial domain. This is a clear limitation when modeling extremes over large geographical domains, but surprisingly, it has been mostly overlooked in the literature. In this paper, we develop a more realistic Bayesian framework based on a novel Gaussian scale mixture model, where the Gaussian process component is defined by a stochastic partial differential equation that yields a sparse precision matrix, and the random scale component is modeled as a low-rank Pareto-tailed or Weibull-tailed spatial process determined by compactly supported basis functions. We show that our proposed model is approximately tail-stationary despite its non-stationary construction in terms of basis functions, and we demonstrate that it can capture a wide range of extremal dependence structures as a function of distance. Furthermore, the inherently sparse structure of our spatial model allows fast Bayesian computations, even in high spatial dimensions, based on a customized Markov chain Monte Carlo algorithm, which prioritize calibration in the tail. In our application, we fit our model to analyze heavy monsoon rainfall data in Bangladesh. Our study indicates that the proposed model outperforms some natural alternatives, and that the model fits precipitation extremes satisfactorily well. Finally, we use the fitted model to draw inferences on long-term return levels for marginal precipitation at each site, and for spatial aggregates.

Keywords: Censored inference; Extremal dependence; Heavy rainfall; Low-rank spatial process; Spatial extremes; Spatial-scale mixture; Stochastic partial differential equation.

¹Computer, Electrical and Mathematical Sciences and Engineering (CEMSE) Division, King Abdullah University of Science and Technology (KAUST), Thuwal 23955-6900, Saudi Arabia.
E-mail: arnab.hazra@kaust.edu.sa

1 Introduction

Extreme weather and climate conditions, e.g., the 2003 or 2011 European heatwaves (Stott et al., 2004; Zhong et al., 2021), extreme rainfall from Hurricane Harvey in Texas, US, in 2017 (Van Oldenborgh et al., 2017), and the extreme winter blackout in Texas, US, in 2021 (Busby et al., 2021), have raised major concerns about serious climate risks among scientists and various stakeholders over the last decades. Climate risk assessment is indispensable in many practical applications (Kharin et al., 2007; Kao and Ganguly, 2011; Ghosh et al., 2012) and is especially relevant in the context of climate change; see the International Panel on Climatic Change (IPCC) reports (Shukla et al., 2019; Masson-Delmotte et al., 2021) and the 2021 COP26 conference goals (Calliari et al., 2020). Recently, Chen et al. (2018) have emphasized the need to build resilient statistical models for analyzing climate extremes. In the spatial extremes literature, however, existing extreme-value models are often deliberately and conveniently applied to low-dimensional spatial datasets observed over relatively small regions (Smith, 1990; Padoan et al., 2010; Davison et al., 2012, 2019; Huser and Wadsworth, 2020), mainly for computational reasons, but also because classical spatial extreme-value models often lack flexibility to capture key data characteristics realistically. In our big data era, and with the availability of massive gridded datasets (e.g., satellite-derived data products, climate model outputs, etc.), it is often needed to model complex high-dimensional extremes observed over large geographical regions and this requires models that transcend the classical extreme-value paradigm.

To model massive and complex spatiotemporal datasets of extremes, two general criteria need to be fulfilled: first, realistic modeling of key marginal and dependence features that determine and impact risk assessment, and second, fast and scalable inference. In the context of extremes, the first criterion requires flexible, yet well-theoretically supported models that capture heavy tails, short-range extremal dependence, mid-range extremal independence, and long-range full independence (as suggested by the first law of geography). Mathematically, extremal dependence between two random variables $Y_1 \sim F_1$ and $Y_2 \sim F_2$ is usually described

in terms of the tail correlation coefficient ([Sibuya, 1960](#)), $\chi = \lim_{u \rightarrow 1} \chi_u$, where

$$\chi_u = \Pr \{Y_1 > F_1^{-1}(u) \mid Y_2 > F_2^{-1}(u)\}; \quad (1)$$

here, $\chi \in (0, 1]$ indicates asymptotic dependence (AD) and $\chi = 0$ indicates asymptotic independence (AI). For a spatial process, the χ -measure between two locations \mathbf{s}_1 and \mathbf{s}_2 is defined by a function $\chi(\mathbf{s}_1, \mathbf{s}_2)$. In order to judge the first criterion in terms of $\chi(\mathbf{s}_1, \mathbf{s}_2)$, we need models that allow joint tail characteristics to be theoretically derived in a closed form. As for the second criterion, we strongly believe that it cannot be achieved without imposing a sparse probabilistic structure to the model. For aggregated risk assessment over complex domain, a third criterion is desired: straightforward and fast simulation and conditional simulation from the estimated model.

Classical spatial extreme-value models usually fall short in at least two, if not the three above criteria. They can essentially be divided into two broad categories: first, models for site-wise block-maxima using max-stable processes. Some examples include the Smith model ([Smith, 1990](#)), Schlather model ([Schlather, 2002](#)), Brown-Resnick model ([Brown and Resnick, 1977](#); [Kabluchko et al., 2009](#)), Reich-Shaby model ([Reich and Shaby, 2012](#)) and extremal- t model ([Opitz, 2013](#)). These models have certain downsides; they are limited to low dimensions (except Reich-Shaby model) and not easily scalable to high dimensions, they are not fully realistic as these models exhibit AD or exact independence, and usually assume AD across the entire spatial domain. Second, peaks over some high thresholds are modeled using generalized Pareto processes ([Dombry and Ribatet, 2015](#); [Thibaud and Opitz, 2015](#); [de Fondeville and Davison, 2018](#)). They are theoretically equivalent models with max-stable processes in case we treat high-threshold exceedances instead of block-maxima as extremes. The main disadvantage of these models is their limited applicability in high-dimensional problems due to multivariate censoring. Some progress has recently been made to fit high-dimensional multivariate Pareto distributions constructed from conditional independence relationships ([Engelke and Hitz, 2020](#)). However, currently, there is no spatial version of these sparse graphical multivariate Pareto models. The conditional spatial extremes model of [Wadsworth and Tawn](#)

(2019) is applicable for higher-dimensional problems and the asymptotic theory is formed through conditioning upon the value at a particular site being extreme. The main downside of this approach is that there is no ‘unconditional representation’ and thus, it lacks a convenient, “physical” interpretation. Also, as originally defined, the model does not have a sparse probabilistic structure, though such a sparse approach has been recently advocated in Simpson et al. (2020). The downsides of the classical models motivate several researchers to consider models based on location and/or scale mixtures of Gaussian processes (Huser et al., 2017; Morris et al., 2017; Krupskii et al., 2018; Hazra et al., 2018, 2020); Huser and Wadsworth (2020) review such approaches. These models are more flexible at sub-asymptotic levels, and in some cases (e.g., Huser et al., 2017), they capture AD or AI within the same modeling framework. However, they are very often constructed from common latent factors that hit all spatial locations simultaneously (e.g., Huser et al., 2017; Krupskii et al., 2018), which thus implies that independence cannot be captured at large distances, a major limitation with large geographical domains. Related to this, these models usually assume either asymptotic dependence for all pairs of sites, or asymptotic independence for all pairs of sites, but cannot capture a change of extremal dependence regime as a function of distance between sites (which is more realistic). Unlike the other sub-asymptotic approaches, the model proposed by Morris et al. (2017) is the only model that is tenable for a large geographical domain as it satisfies the short-range extremal dependence and long-range independence property (although in a limiting sense). Following Kim et al. (2005), Morris et al. (2017) consider random spatial partitioning of the spatial domain based on Voronoi tessellation (Green and Sibson, 1978), followed by considering separate random location and scale terms of the underlying GP within each part. The long-range extremal independence is satisfied *almost surely* only when we allow an unconstrained number of partitions, but Morris et al. (2017) fix the number of partitions for computation, and hence the asymptotic justification can never be fully achieved. Besides, the partitioning idea of Kim et al. (2005) is motivated by sharply changing spatial covariance structure, and similarly would lead to sharply changing extremal dependence in

the context of [Morris et al. \(2017\)](#). Additionally, the model involves the imputation of the partition indexes for each spatial location within each Markov chain Monte Carlo (MCMC) step, which is computationally challenging.

Our approach is to build upon existing Gaussian scale mixture models for several reasons. These models have a natural link to standard geostatistics approaches, it is easy to perform simulation and conditional simulation for these models, they allow relatively fast inference, and Gaussian scale mixtures can capture AI and AD depending on the tail of the mixing variable. One specific example of such models is the model proposed by [Huser et al. \(2017\)](#) (the so-called “HOT model”), which is detailed in [Section 2](#). The HOT model is a copula model where the underlying spatial process is obtained by multiplying a standard dense Gaussian process by a random latent scale variable which bridges two probability distributions, namely, Pareto and Weibull, and leads to the two classes AD and AI, respectively. In this paper, we propose an extension of the HOT model (called the “SHOT model” for “Spatial HOT model”) that improves the HOT model in several important ways: *first*, we replace the one common latent random scale (hence, only a single shock) for the whole spatial domain by a random spatial process. This is motivated by the fact that a geographical shock is generally a local phenomenon (a cyclone generally affects only the coastal regions, for example), and spatially-varying shocks allow us to capture AD at short distances, AI at large distances, and complete independence at infinite distances. *Second*, for computational suitability, we assume the random scaling process to be of the low-rank structure, constructed from a nonlinear spatially-varying combination of a set of random shocks that allow stationary marginal tails. *Third*, we consider the underlying Gaussian process to be a Gaussian Markov random field (GMRF, [Rue and Held, 2005](#)), where the construction is based on stochastic partial differential equations that allow a sparse probabilistic structure scalable to high dimensions. *Fourth*, while HOT is only a copula model, we model the margins and the dependence both in a unified approach; we also incorporate spatially-varying location parameters for additional flexibility in fitting the marginal distributions. While the margins do not follow the GEV distribution,

joint modeling of the margins and dependence is a more natural modeling approach, and better for overall uncertainty assessment. Further, we discuss the properties of the model and Bayesian computational details using MCMC. Inclusion of a nugget effect in the construction of the underlying GMRF allows fast imputation of the censored observations below certain high thresholds, and the spatially-varying parameters and many latent variables allow Gibbs sampling. We compare the proposed model with some natural alternatives using deviance information criterion (DIC).

We fit the proposed model to analyze heavy rainfall in Bangladesh. We choose daily precipitation data obtained from the project Tropical Rainfall Measuring Mission (TRMM Version 7) available over the period March 2000 through December 2019 at a spatial resolution of $0.25^\circ \times 0.25^\circ$. Focusing on heavy rainfall that affects monsoon crops, from an agroclimatological perspective, we keep data only for the months June through September. Overall, the final dataset contains observations at 195 grid cells for 2440 days. We draw posterior inferences about one-year, five-year, and ten-year return levels at each grid cell. Considering the six regions defined by [Mannan and Karmakar \(2007\)](#) in the context of heavy rainfall analysis in Bangladesh, we also draw some regional inferences.

The paper is organized as follows. In §2, we begin with a summary of the model proposed by [Huser et al. \(2017\)](#), then we describe the Gaussian spatial scale mixture process, and finally, we discuss some theoretical properties of the proposed model. Bayesian computational details are discussed in §3. In §4, we discuss some results obtained from a simulation study. We fit the proposed model to analyze heavy precipitation in Bangladesh and discuss the results in §5. §6 concludes.

2 Gaussian spatial scale mixture process

2.1 Gaussian single scale mixture process

In this subsection, we briefly describe the Gaussian single scale mixture process proposed by [Huser et al. \(2017\)](#) (HOT, thereafter). The authors transform the temporal replications

of the observed spatial field into a pseudo-uniform marginal scale station-wise, using rank transformations, and model the underlying spatial dependence structure by a copula generated through a spatial process $W(\cdot)$ defined as

$$W(\mathbf{s}) = RZ(\mathbf{s}), \quad \mathbf{s} \in \mathcal{D} \subset \mathbb{R}^2, \quad (2)$$

where $Z(\cdot)$ is a standard GP with some correlation structure $\text{Cor}[Z(\mathbf{s}_1), Z(\mathbf{s}_2)] = \rho(\mathbf{s}_1, \mathbf{s}_2)$, R and $Z(\cdot)$ are independent, and $R \sim F_{\beta, \gamma}$, a two-parameter probability distribution, given by

$$F_{\beta, \gamma}(r) = \begin{cases} 1 - \exp\{-\gamma(r^\beta - 1)/\beta\} & \text{if } \beta > 0, \\ 1 - r^{-\gamma} & \text{if } \beta = 0, \end{cases} \quad r \in [1, \infty). \quad (3)$$

This specific characterization of $F_{\beta, \gamma}$ is motivated by different bivariate tail behaviors of $W(\cdot)$. Suppose, $C(u_1, u_2)$ denotes the bivariate copula of $[W(\mathbf{s}_1), W(\mathbf{s}_2)]'$, and $\bar{C}(u_1, u_2) = 1 - u_1 - u_2 + C(u_1, u_2)$ denotes the corresponding survival copula. Then, additional to χ -measure described in Section 1, Coles et al. (1999) also consider $\bar{\chi}$ for characterizing the bivariate joint tail-decay of $[W(\mathbf{s}_1), W(\mathbf{s}_2)]'$, where, $\bar{\chi} = \lim_{u \rightarrow 1} \bar{\chi}_u$ and for $u \approx 1$,

$$\chi_u = 2 - \frac{\log(C(u, u))}{\log(u)}, \quad \bar{\chi}_u = \frac{2 \log(1 - u)}{\log(\bar{C}(u, u))} - 1. \quad (4)$$

Similar to different regimes based on χ , $W(\mathbf{s}_1)$ and $W(\mathbf{s}_2)$ exhibit extremal dependence when $\bar{\chi} = 1$, and extremal independence when $\bar{\chi} \in (-1, 1)$. When we have $\beta > 0$ in (3), we obtain extremal independence with

$$\chi = 0 \quad \text{and} \quad \bar{\chi} = 2\{(1 + \rho(\mathbf{s}_1, \mathbf{s}_2))/2\}^{\beta/(\beta+2)} - 1.$$

In case $\beta = 0$, we obtain extremal dependence with

$$\bar{\chi} = 1 \quad \text{and} \quad \chi = 2\bar{F}_T(\{(\gamma + 1)(1 - \rho(\mathbf{s}_1, \mathbf{s}_2))/(1 + \rho(\mathbf{s}_1, \mathbf{s}_2))\}^{1/2}; \gamma + 1),$$

where $F_T(\cdot; a)$ is the Student's t -distribution function with a degrees of freedom. The main benefit of this model over other related approaches (including those who consider location and scale mixtures) is due to the smooth transition between the two asymptotic regimes as $\beta \downarrow 0$. However, by considering a single R for the whole spatial domain, the model automatically assumes that the whole process is either asymptotically dependent or asymptotically independent, and hence, cannot exhibit two different regimes for nearby and far locations.

2.2 SHOT: Gaussian spatial scale mixture process

Here, first, we describe the dependence structure modeling, and subsequently, we will discuss the full model specification for the observed data. Instead of $W(\cdot)$ in (2), we consider a GP with a stochastic scale process (abbreviated as spatial HOT or SHOT, henceforth) defined as

$$X(\mathbf{s}) = R(\mathbf{s})Z(\mathbf{s}), \quad \mathbf{s} \in \mathcal{D} \subset \mathbb{R}^2, \quad (5)$$

where $Z(\cdot)$ is a standard GP with correlation structure $\text{Cor}[Z(\mathbf{s}_1), Z(\mathbf{s}_2)] = \rho(\mathbf{s}_1, \mathbf{s}_2)$, $R(\mathbf{s})$ is positive *with probability one*, for all $\mathbf{s} \in \mathcal{D}$, and $R(\cdot)$ and $Z(\cdot)$ are independent processes. Conditional on $R(\cdot)$, the process $X(\cdot)$ is Gaussian, with the correlation structure same as that of $Z(\cdot)$, and the marginal standard deviations are spatially-varying, with $\text{SD}[X(\mathbf{s})] = R(\mathbf{s})$. If $R(\mathbf{s}) = R_0$ *almost surely* for all $\mathbf{s} \in \mathcal{D}$ for some $R_0 \in \mathbb{R}^+$, then the resulting unconditional process is a stationary GP. Our goal is to construct the processes $R(\cdot)$ and $Z(\cdot)$ in such a way that the process $X(\cdot)$ is tail-stationary (approximately), that is, $\Pr(X(\mathbf{s}) > x)$ is independent of \mathbf{s} for large x , and its χ -measure, $\chi_X(\mathbf{s}_1, \mathbf{s}_2)$ is stationary (in a limiting sense). For $W(\cdot)$ in (2), these properties are automatically satisfied assuming $\rho(\mathbf{s}_1, \mathbf{s}_2)$ to be stationary. The model proposed by Morris et al. (2017) is also tail-stationary (in a limiting sense, assuming infinitely many partitions in their random spatial partitioning approach).

2.2.1 Construction of $Z(\cdot)$

We assume that the process $Z(\cdot)$ has an isotropic Matérn spatial correlation given by

$$\rho(\mathbf{s}_1, \mathbf{s}_2) = \frac{r}{\Gamma(\nu)2^{\nu-1}} \left(\frac{d(\mathbf{s}_1, \mathbf{s}_2)}{\psi} \right)^\nu K_\nu \left(\frac{d(\mathbf{s}_1, \mathbf{s}_2)}{\psi} \right) + (1-r)\mathbb{I}(\mathbf{s}_1 = \mathbf{s}_2), \quad (6)$$

where $d(\mathbf{s}_1, \mathbf{s}_2)$ is the Euclidean distance (in degrees) between \mathbf{s}_1 and \mathbf{s}_2 (thereafter), $\psi > 0$, $\nu > 0$ and $r \in [0, 1]$ are range, smoothness, and the ratio of spatial to total variation, respectively. In (6), K_ν is the modified Bessel function of degree ν , and $\mathbb{I}(\mathbf{s}_1 = \mathbf{s}_2) = 1$ if $\mathbf{s}_1 = \mathbf{s}_2$, and 0 otherwise. An integer value of ν determines the mean-square differentiability of $Z(\cdot)$ when $r = 1$. However, ν is often fixed because it is poorly identified in the data applications. Here, we fix $\nu = 1$. Instead of considering a dense GP with the spatial correlation

in (6), we consider the process $Z(\cdot)$ to be an approximately stationary Gaussian Markov random field (GMRF), exploiting the link between a dense GP and a GMRF described in Lindgren et al. (2011).

Suppose, $\varepsilon(\cdot)$ is a dense GP with the spatial correlation structure (6), with $r = 1$. Then, $\varepsilon(\cdot)$ a solution to the linear fractional stochastic partial differential equation (SPDE)

$$(8\psi^{-2} - \Delta)\varepsilon(\mathbf{s}) = \mathcal{W}(\mathbf{s}), \quad \mathbf{s} \in \mathbb{R}^d,$$

where $\mathcal{W}(\mathbf{s})$ is Gaussian white noise, and $\Delta = \frac{\delta^2}{\delta^2 x} + \frac{\delta^2}{\delta^2 y}$ is the Laplacian operator. The SPDE is then solved using finite element methods (Ciarlet, 2002) over a triangular mesh on a bounded domain in \mathbb{R}^2 , where the triangles are formed as a refined Delaunay triangulation, implemented in the function `inla.mesh.2d` from the R package INLA (www.r-inla.org); see Lindgren and Rue (2015). The mesh we consider for the data application in Section 5 is presented in the left panel of Figure 1. Suppose, the data are observed at the spatial locations $\mathcal{S} = \{\mathbf{s}_1, \dots, \mathbf{s}_N\}$, and the set of mesh nodes is denoted by $\mathcal{S}^* = \{\mathbf{s}_1^*, \dots, \mathbf{s}_{N^*}^*\}$. We construct a finite element representation of the solution to $\varepsilon(\mathbf{s}) = \sum_{j=1}^{N^*} \phi_j(\mathbf{s})\varepsilon_j^*$ for the piecewise linear basis functions $\phi_j(\cdot)$ defined by the mesh and normally distributed weights ε_j^* defined at the mesh nodes \mathcal{S}^* . We calculate the inner products $\langle \phi_j(\cdot), 1 \rangle$ and $\langle \nabla \phi_{j_1}(\cdot), \nabla \phi_{j_2}(\cdot) \rangle$, where $\langle f, g \rangle = \int f(\mathbf{s})g(\mathbf{s})d\mathbf{s}$, and obtain the corresponding $(N^* \times N^*)$ -dimensional finite element matrices \mathbf{C} , \mathbf{G}_1 , and \mathbf{G}_2 , where \mathbf{C} is a diagonal matrix with its $(j, j)^{th}$ entry $C_{j,j} = \langle \phi_j(\cdot), 1 \rangle$, \mathbf{G}_1 is a sparse matrix with its $(j_1, j_2)^{th}$ entry $G_{j_1, j_2} = \langle \nabla \phi_{j_1}(\cdot), \nabla \phi_{j_2}(\cdot) \rangle$, and $\mathbf{G}_2 = \mathbf{G}_1 \mathbf{C}^{-1} \mathbf{G}_1$; this procedure is implemented in the function `inla.mesh.fem` from the R package INLA. Further theoretical details are discussed in Bakka et al. (2018) and Lindgren et al. (2021). Finally, the vector $\boldsymbol{\varepsilon}^* = [\varepsilon_1^*, \dots, \varepsilon_{N^*}^*]'$ follows the distribution $\boldsymbol{\varepsilon}^* \sim \text{Normal}_{N^*}(\mathbf{0}, \mathbf{Q}_\psi^{-1})$, where the precision matrix \mathbf{Q}_ψ is given by

$$\mathbf{Q}_\psi = \frac{\psi^2}{4\pi} \left[\frac{1}{\psi^4} \mathbf{C} + \frac{2}{\psi^2} \mathbf{G}_1 + \mathbf{G}_2 \right]. \quad (7)$$

While $\boldsymbol{\varepsilon}^*$ is defined over the mesh nodes and its elements denote the spatial random effects, to obtain the spatial field, we need to multiply them by the basis functions $\phi_j(\cdot)$'s. To project

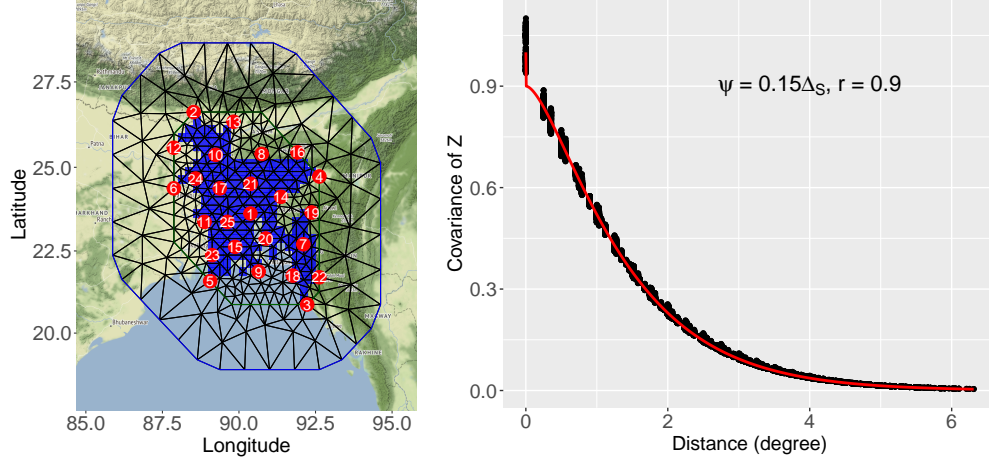


Figure 1: Left: Triangulated mesh over Bangladesh, that is used to construct the spatial process $Z(\cdot)$, using SPDE. The red dots denote the spatial knot locations \mathcal{S}^* used in the construction of the random scale process $R(\cdot)$. Right: Comparison of the true Matérn correlation and the pairwise covariances between two spatial locations obtained by SPDE approximation, as a function of distance. The parameter choices are $\psi = 0.15\Delta_{\mathcal{S}}$ and $r = 0.9$.

$\boldsymbol{\varepsilon}^*$ back to the observation locations \mathcal{S} , we calculate $\phi_j(\mathbf{s}_i)$ for each spatial location \mathbf{s}_i and the mesh node \mathbf{s}_j^* . Suppose, \mathbf{A} denotes the SPDE projection matrix from \mathcal{S}^* to \mathcal{S} . Then, the $(i, j)^{th}$ element of \mathbf{A} is equal to $\phi_j(\mathbf{s}_i)$; the evaluation of the matrix \mathbf{A} is implemented in the function `inla.spde.make.A` from the R package `INLA`.

Suppose, $\mathbf{Z} = [Z(\mathbf{s}_1), \dots, Z(\mathbf{s}_N)]'$. We link the vectors \mathbf{Z} and $\boldsymbol{\varepsilon}^*$ by

$$\mathbf{Z} = \sqrt{r}\mathbf{A}\boldsymbol{\varepsilon}^* + \sqrt{1-r}\boldsymbol{\eta}, \quad (8)$$

where \mathbf{A} denotes the SPDE projection matrix, and $\boldsymbol{\eta} = [\eta(\mathbf{s}_1), \dots, \eta(\mathbf{s}_N)]'$ with $\eta(\mathbf{s}_i) \stackrel{\text{iid}}{\sim} \text{Normal}(0, 1)$. The final covariance matrix of \mathbf{Z} is $\Sigma_{\mathbf{Z}} = r\mathbf{A}\mathbf{Q}_{\psi}^{-1}\mathbf{A}' + (1-r)\mathbf{I}_N$, and it approximates the Matérn correlation matrix with range ψ , the ratio of partial sill to total variation r , and the smoothness parameter $\nu = 1$.

As an illustration of the approximation, we choose $\psi = 0.15\Delta_{\mathcal{S}}$ and $r = 0.9$, where $\Delta_{\mathcal{S}}$ denotes the maximum of the Euclidean distances between two spatial locations. Considering the SPDE mesh presented in the left panel of Figure 1, we calculate the approximated covariance between every pair of spatial locations (the elements of the matrix $\Sigma_{\mathbf{Z}}$) and the corresponding true Matérn correlation based on (6), and present them in the right panel of

Figure 1, as a function of distance. We observe that the true correlation of the dense GP is well approximated by the GMRF. We exploit the sparsity of the matrix \mathbf{Q}_ψ to allow fast computation. Additionally, while considering censoring, we exploit the conditional spatial independence structure $\mathbf{Z}|\boldsymbol{\varepsilon}^* \sim \text{Normal}_N(\sqrt{r}\mathbf{A}\boldsymbol{\varepsilon}^*, (1-r)\mathbf{I}_N)$, that allows univariate imputations of censored data.

2.2.2 Construction of $R(\cdot)$

For the process $R(\cdot)$, we consider a low-rank representation

$$R(\mathbf{s}) = \left[1 + \beta \log \left\{ \sum_{k=1}^K B_k^{1/\gamma}(\mathbf{s}; \phi) \exp \left(\frac{R_k^* \beta - 1}{\beta} \right) \right\} \right]^{1/\beta}, \quad \beta > 0, \quad (9)$$

where $R_k^*; k = 1, \dots, K \stackrel{\text{iid}}{\sim} F_{\beta, \gamma}$, with $F_{\beta, \gamma}$ is as in (3), and the parameters β and γ have same interpretation as in (3). The fixed and compactly supported spatial basis functions $B_k(\mathbf{s}; \phi), k = 1, \dots, K$ satisfy the constraint $\sum_{k=1}^K B_k(\mathbf{s}; \phi) = 1$, for each $\mathbf{s} \in \mathcal{S}$. For $K = 1$ in (9), the model (5) coincides with (2). For $\beta = 0$, $R(\mathbf{s})$ is defined as a limit ($\beta \downarrow 0$) by $R(\mathbf{s}) = \sum_{k=1}^K B_k^{1/\gamma}(\mathbf{s}; \phi) R_k^*$, where $R_k^*; k = 1, \dots, K \stackrel{\text{iid}}{\sim} F_{0, \gamma}$. The choice of K is problem-specific and involves a trade-off between the approximation to a tail-stationary behavior and the computational burden. In our simulation studies and the data application, we consider a few different choices of K and select the most optimal choice based on cross-validation.

Further, we discuss the construction of $B_k(\mathbf{s}; \phi)$. To allow the stochastic process (5) to have extremal dependence only at the short distances, we choose compactly supported Wendland basis functions over \mathbb{R}^2 and of order 2 (implemented in the function `Wendland2.2` from the R package `fields`), with the range parameter ϕ , and given by the expression

$$C_k(\mathbf{s}; \phi) = \left(1 - \frac{d(\mathbf{s}, \tilde{\mathbf{s}}_k^*)}{\phi} \right)^6 \left(35 \frac{d(\mathbf{s}, \tilde{\mathbf{s}}_k^*)^2}{\phi^2} + 18 \frac{d(\mathbf{s}, \tilde{\mathbf{s}}_k^*)}{\phi} + 3 \right) \mathbb{I}(d(\mathbf{s}, \tilde{\mathbf{s}}_k^*) < \phi), \quad (10)$$

where $\tilde{\mathcal{S}} = \{\tilde{\mathbf{s}}_1^*, \dots, \tilde{\mathbf{s}}_K^*\} \subset \mathcal{S}^*$ denotes the set of K spatial knot locations. Further, we evaluate $C_k(\mathbf{s}; \phi)$ at the data locations \mathcal{S} and form the $(N \times K)$ -dimensional matrix \mathbf{C} , where the (i, k) -th entry is $C_k(\mathbf{s}_i; \phi)$. Subsequently, we scale $C_k(\mathbf{s}_i; \phi)$'s at each \mathbf{s}_i to obtain $B_k(\mathbf{s}_i; \phi) = C_k(\mathbf{s}_i; \phi) / \sum_{k_0=1}^K C_{k_0}(\mathbf{s}_i; \phi)$ that ensures $\sum_{k=1}^K B_k(\mathbf{s}; \phi) = 1$, and $B_k(\mathbf{s}_i; \phi), k = 1, \dots, K$ are

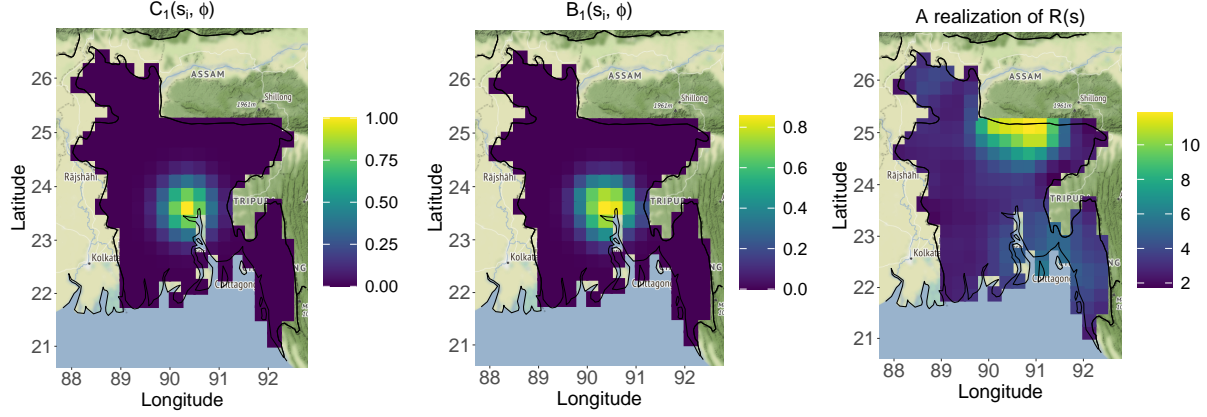


Figure 2: Left: Wendland basis function $C_1(\mathbf{s}_i; \phi)$ evaluated at the data locations \mathcal{S} . Middle: The corresponding rescaled Wendland basis function $B_1(\mathbf{s}_i; \phi)$. Right: A simulated realization of the process $R(\cdot)$ at the data locations. The parameter choices in (9) are $\beta = 0$, $\gamma = 2.5$, and $\phi = 1.5$, with $K = 25$.

used to obtain $R(\mathbf{s}_i)$ using (9). We select the K knot locations from $\mathcal{S}^{*(c)} = \cup_{\{\mathbf{s}_i \in \mathcal{S}\}} \{\mathbf{s}_j^* \in \mathcal{S}^* | d(\mathbf{s}_i, \mathbf{s}_j^*) \leq c \cdot \max_{\mathbf{s}_{j_0}^* \in \mathcal{S}^*} d(\mathbf{s}_i, \mathbf{s}_{j_0}^*)\} \subseteq \mathcal{S}^*$ (the set of mesh nodes that are within a certain distance from the data locations), using the maximum-minimum ordering, introduced by Guinness (2018), in the context of Vecchia approximation of the Gaussian process likelihood. If $c = 1$, we have $\mathcal{S}^{*(c)} = \mathcal{S}^*$. For our data application, we fix $c = 0.05$. For $K = 25$, we illustrate the ordering in the left panel of Figure 1. The first knot location is selected in such a way that the corresponding mesh node has the least average distance to the other mesh nodes. Subsequently, we select the j -th mesh node from $\mathcal{S}^{*(c)}$ as the k -th knot location if

$$j = \arg \max_{\{j_0 | \mathbf{s}_{j_0}^* \in \mathcal{S}^{*(c)} \setminus \{\tilde{\mathbf{s}}_1^*, \dots, \tilde{\mathbf{s}}_{k-1}^*\}\}} \min_{k_0 \in \{1, \dots, k-1\}} d(\mathbf{s}_{j_0}^*, \tilde{\mathbf{s}}_{k_0}^*).$$

For $K = 25$, we illustrate $C_1(\mathbf{s}_i; \phi)$, $B_1(\mathbf{s}_i; \phi)$, and a realization of $R(\mathbf{s}_i)$ for $\phi = 1.5$ at all $\mathbf{s}_i \in \mathcal{S}$, in Figure 2. The compactness of $B_1(\mathbf{s}_i; \phi)$ is clear from the middle panel, and hence its corresponding random coefficient impact only the observations in the central region, allowing local shocks. The realization of $R(\cdot)$ illustrates that the proposed construction allows spatially-varying $R(\cdot)$ instead of a fixed R throughout the domain \mathcal{S} as in (2). Besides, large values only near the northeastern region (Himalayan foothills) illustrates that the model can capture natural behaviors of the studied stochastic process (precipitation field, for example).

2.2.3 Full model specification

While (5) describes the spatial dependence modeling, the process $Z(\cdot)$ is (approximately) stationary, and the scale process $R(\cdot)$ is also tail-stationary (discussed later in Section 2.3). As a result, the product process $X(\cdot)$ is also tail-stationary. To allow additional flexibility in the marginal tails (while the spatial extremal dependence to be determined by $X(\cdot)$) of the observed data $\mathcal{Y} = \{Y_t(\mathbf{s}_i), \mathbf{s}_i \in \mathcal{S}, t = 1, \dots, T\}$, we propose the full model

$$Y_t(\mathbf{s}_i) = \mu(\mathbf{s}_i) + \tau^{-1/2}X_t(\mathbf{s}_i), \quad (11)$$

where $\mu(\cdot)$ is a spatially varying mean surface, τ denotes a spatially invariant precision parameter, and $X_t(\cdot)$ is a replication of the stochastic process $X(\cdot)$ in (5). The observations are assumed to be independent across time $t = 1, \dots, T$. Instead of fitting the model (11) to the whole dataset \mathcal{Y} , we choose site-specific thresholds (0.95th data quantile, at each site, for example), and fit the model (11) only to the threshold exceedances, and treat the values below the thresholds as censored responses to be imputed using Bayesian computing. The t -th replications of ϵ^* in (8) and of R_k^* in (9) are denoted by ϵ_t^* and $R_{k,t}^*$, respectively, for $t = 1, \dots, T$.

2.3 Model properties

Here, first we discuss the tail properties of the scale process $R(\cdot)$, and then for the product process $X(\cdot)$. Our main focus is on the χ -measure, described in (4), when $\beta = 0$. When $\beta > 0$, the χ -measure of the process $X(\cdot)$ between any two spatial location is zero, follows from Huser et al. (2017) and the fact that the process $X(\cdot)$ in (5) exhibits weaker tail dependence than that of $W(\cdot)$ in (2).

Theorem 1. *For any $\beta \geq 0$, The process $R(\cdot)$ is tail-stationary, that is,*

$$\lim_{r \uparrow \infty} \frac{\Pr(R(\mathbf{s}_1) > r)}{\Pr(R(\mathbf{s}_2) > r)} = 1, \quad \forall \mathbf{s}_1, \mathbf{s}_2 \in \mathcal{S}$$

A theoretical proof is provided in the Supplementary Material. As a corollary of Theorem 1, we have $\lim_{x \uparrow \infty} \Pr(X(\mathbf{s}_1) > x) / \Pr(X(\mathbf{s}_2) > x) = 1$ for all $\mathbf{s}_1, \mathbf{s}_2 \in \mathcal{S}$, follows

from $X(\mathbf{s}_1) = R(\mathbf{s}_1)Z(\mathbf{s}_1)$ and $X(\mathbf{s}_2) = R(\mathbf{s}_2)Z(\mathbf{s}_2)$, and $Z(\mathbf{s}_1), Z(\mathbf{s}_2) \sim \text{Normal}(0, 1)$, approximately (GMRF approximation of dense GP). A formal proof follows directly from the Breiman's theorem (Breiman, 1965), as $E(|Z(\mathbf{s})|^\alpha)$ is finite for any finite $\alpha > 0$.

Theorem 2. For $\beta = 0$, the extremal dependence coefficient (χ , defined in (4)) of $R(\cdot)$ is

$$\chi_R(\mathbf{s}_1, \mathbf{s}_2) = \sum_{k=1}^K \min\{B_k(\mathbf{s}_1; \phi), B_k(\mathbf{s}_2; \phi)\}.$$

A theoretical proof is provided in the Supplementary Material. The extremal dependence $\chi_R(\mathbf{s}_1, \mathbf{s}_2)$ is independent of γ , $\chi_R(\mathbf{s}, \mathbf{s}) = 1$, and if no basis function *covers* both \mathbf{s}_1 and \mathbf{s}_2 , then $\chi_R(\mathbf{s}_1, \mathbf{s}_2) = 0$. Because of considering compactly supported basis functions $B_k(\cdot, \phi)$, the parameter ϕ controls the strength as well as the range of the spatial extremal dependence.

In order to ensure $B_k(\mathbf{s}_i; \phi)$ is finite for each i and k , $\min_i \max_k C_k(\mathbf{s}_i, \phi) > 0$ is a necessary criterion, as otherwise $C_k(\mathbf{s}_i, \phi)$ would be zero for all k , for some $\mathbf{s}_i \in \mathcal{S}$. If $\max_k \min_i C_k(\mathbf{s}_i, \phi) > 0$, then any two spatial observation locations are *covered* by at least one basis function resulting in $\chi_R(\mathbf{s}_1, \mathbf{s}_2) > 0$ for any $\mathbf{s}_1, \mathbf{s}_2 \in \mathcal{S}$. These two criteria are equivalent to $\phi > \phi_{\min}$ and $\phi > \phi_{\max}$, respectively, where $\phi_{\min} = \max_i \min_k d(\mathbf{s}_i, \tilde{\mathbf{s}}_k^*)$ and $\phi_{\max} = \min_k \max_i d(\mathbf{s}_i, \tilde{\mathbf{s}}_k^*)$. For the mesh nodes and the spatial knot locations presented in the left panel of Figure 1, we have $\phi_{\min} = 0.76$ degrees and $\phi_{\max} = 3.26$ degrees. When we choose all the mesh nodes as knots, that is, $\mathcal{S}^{*(c)} = \mathcal{S}^*$ and $K = N^*$, we have $\phi_{\min} = 0.25$ degrees and $\phi_{\max} = 3.20$ degrees. Additionally, if $\mathcal{S} \subseteq \mathcal{S}^*$, we have $\phi_{\min} = 0$ degree. Further, if we choose $K = 25$ but set $\mathcal{S}^{*(c)} = \mathcal{S}^*$, we have $\phi_{\min} = 1.46$ degrees and $\phi_{\max} = 3.26$ degrees.

For illustration, we choose $\phi = 3, 6$, with (i) $K = 25$ and $c = 1$, (ii) $K = N^*$ and $c = 1$, and (iii) $K = 25$ and $\mathcal{S}^{*(c)} \subset \mathcal{S}$ with $c = 0.05$, and present $\chi_R(\mathbf{s}_1, \mathbf{s}_2)$ as a function of $d(\mathbf{s}_1, \mathbf{s}_2)$, in Figure 3. When $\phi = 3$ (between ϕ_{\min} and ϕ_{\max} for all the cases), χ_R is exactly zero for large distances (the exact range of spatial extremal dependence is not the same as ϕ , and depends on the SPDE approximation) for both the choices of K . When $K = 25$ and $c = 1$, the χ_R profile is far from stationarity, but for $K = N^*$ and the same $c = 1$, the profile appears to be fairly stationary. However, while analyzing a real dataset, for the purpose of computing, a

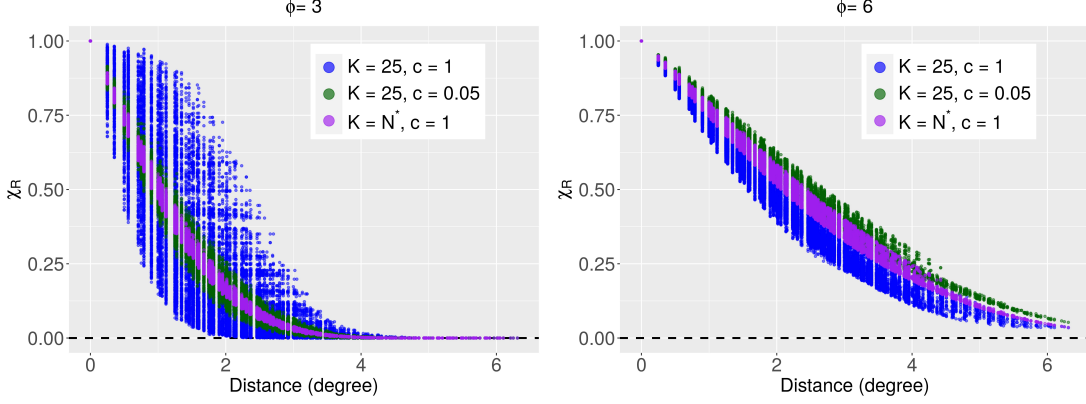


Figure 3: Spatial extremal dependence of the process $R(\cdot)$, when the Wendland basis range parameter $\phi = 3$ (left) and $\phi = 6$ (right) in (10), and under three scenarios: (i) $K = 25$ and $c = 1$, (ii) $K = N^*$ and $c = 1$, and (iii) $K = 25$ and $c = 0.05$.

small value of K ($K = 25$, for example) is required, as otherwise the computation would be infeasible. By choosing $c = 0.05$ and thus, by allowing spatial knot locations to be only within a certain small distance from the observation locations, we observe that the stationarity of χ_R profile is well satisfied even for $K = 25$. Hence, a small value of c is recommended for practical purposes. For $\phi = 6$ (larger than ϕ_{\max} for all the cases), χ_R is nonzero for every pair of the observation locations. Compared to the case of $\phi = 3$, the χ_R profile for $K = 25$ and $c = 1$ show relatively more stationary behavior, while the χ_R values for cases (ii) and (iii) are generally larger in comparison to case (i). The model (2), proposed by Huser et al. (2017), coincides with the case of $K = 1$, where $\chi_R(\mathbf{s}_1, \mathbf{s}_2) = 1$ for any $\mathbf{s}_1, \mathbf{s}_2 \in \mathcal{S}$, and in comparison, the proposed model (5) allows a larger class of χ_R profiles with extremal dependence for short distances and independence for large distances, for suitable choices of ϕ .

Theorem 3. For $\beta = 0$, the extremal dependence coefficient of $X(\cdot)$ is

$$\chi_X(\mathbf{s}_1, \mathbf{s}_2) = \sum_{\substack{\{k: B_k(\mathbf{s}_1; \phi) > 0, \\ B_k(\mathbf{s}_2; \phi) > 0\}}} \left[B_k(\mathbf{s}_1; \phi) \bar{T}_{\gamma+1} \left(\sqrt{\gamma+1} \frac{B_k(\mathbf{s}_1; \phi)^{1/\gamma} B_k(\mathbf{s}_2; \phi)^{-1/\gamma} - \rho(\mathbf{s}_1, \mathbf{s}_2)}{\sqrt{1 - \rho(\mathbf{s}_1, \mathbf{s}_2)^2}} \right) + \right. \\ \left. B_k(\mathbf{s}_2; \phi) \bar{T}_{\gamma+1} \left(\sqrt{\gamma+1} \frac{B_k(\mathbf{s}_2; \phi)^{1/\gamma} B_k(\mathbf{s}_1; \phi)^{-1/\gamma} - \rho(\mathbf{s}_1, \mathbf{s}_2)}{\sqrt{1 - \rho(\mathbf{s}_1, \mathbf{s}_2)^2}} \right) \right],$$

where $\bar{T}_n(\cdot)$ denotes the Student's t survival function with n degrees of freedom.

A theoretical proof is provided in the Supplementary Material. Unlike χ_R , χ_X is dependent

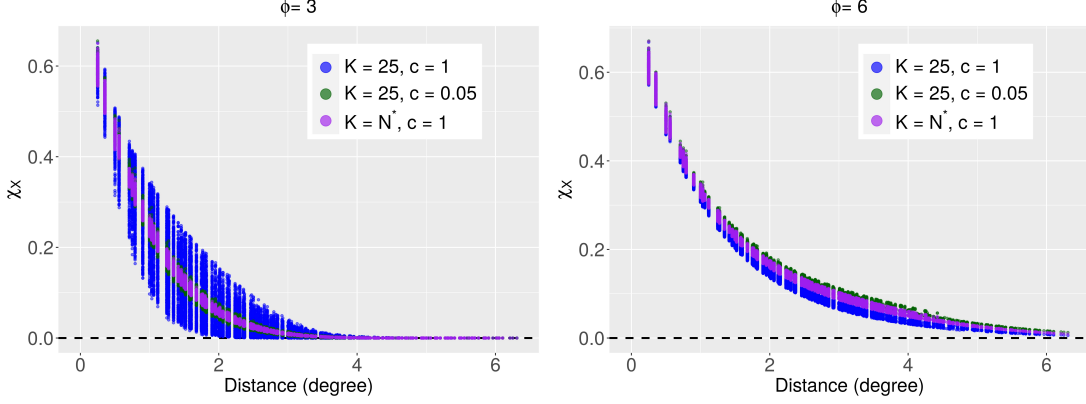


Figure 4: Spatial extremal dependence of the process $X(\cdot)$, when the Wendland basis range parameter $\phi = 3$ (left) and $\phi = 6$ (right) in (10), and under three scenarios: (i) $K = 25$ and $c = 1$, (ii) $K = N^*$ and $c = 1$, and (iii) $K = 25$ and $c = 0.05$. We set $\gamma = 2.5$, $\psi = 0.15\Delta_S$, $r = 0.9$, and $\nu = 1$.

on γ , and also on the spatial correlation (6) of the process $Z(\cdot)$. We have $\chi_X(\mathbf{s}, \mathbf{s}) = 1$, and if no basis function *covers* both \mathbf{s}_1 and \mathbf{s}_2 , then $\chi_X(\mathbf{s}_1, \mathbf{s}_2) = 0$, similar to that of χ_R . The spatial extremal dependence in $X(\cdot)$ is induced by the extremal dependence of $R(\cdot)$, and hence, when $\chi_R(\mathbf{s}_1, \mathbf{s}_2) = 0$, we have $\chi_X(\mathbf{s}_1, \mathbf{s}_2) = 0$. As a result, similar to the case of $R(\cdot)$, the parameter ϕ controls the range of the spatial extremal dependence of $X(\cdot)$.

For illustration, we again choose $\phi = 3, 6$, and the same three cases of K and c as earlier, that is, (i) $K = 25$ and $c = 1$, (ii) $K = N^*$ and $c = 1$, and (iii) $K = 25$ and $\mathcal{S}^{*(c)} \subset \mathcal{S}$ with $c = 0.05$, and present $\chi_X(\mathbf{s}_1, \mathbf{s}_2)$ as a function of $d(\mathbf{s}_1, \mathbf{s}_2)$, in Figure 4. We set $\gamma = 2.5$, and $\psi = 0.15\Delta_S$, $r = 0.9$, and $\nu = 1$ determine $\rho(\mathbf{s}_1, \mathbf{s}_2)$ in (6). When $\phi = 3$, χ_X is exactly zero for large distances for all three cases, and the χ_X profiles exhibit better approximation to a stationary behavior compared to the χ_R profiles. For $\phi = 6$, χ_X is nonzero for every pair of the data locations, similar to χ_R . Here, all the χ_X profiles for the three cases show relatively more stationary behavior compared to the case of $\phi = 3$, while the χ_X values for cases (ii) and (iii) are generally larger in comparison to case (i), similar to the ordering in case of χ_R . While the model of Huser et al. (2017) in (2) can exhibit the spatial extremal dependence χ_W similar to the χ_X profile for $\phi = 6$ (decreasing with distance, stationary, and nonzero throughout the distances) for specific choices of the correlation structure $\rho(\mathbf{s}_1, \mathbf{s}_2)$, χ_W cannot

imitate the pattern of χ_X profile for $\phi = 3$, where the profile is exactly zero for large distances.

3 Computation

We draw posterior inference about the model parameters in (11) using Markov chain Monte Carlo (MCMC) sampling. We fix the SPDE mesh object to be the same as presented in Figure 1, and choose the number of basis functions to be $K = 3^2, 4^2, 5^2, 6^2$ and $\mathcal{S}^{*(c)} \subset \mathcal{S}$ with $c = 0.05$. Here we focus on the case of $\beta = 0$ in (3) and $\phi < \phi_{\max}$ in (10) as this induces short-range extremal dependence and long-range independence. Some results for $\beta > 0$ are provided in the Supplementary Material.

For the parameters involved in the covariance structure (6) of $Z(\cdot)$, we choose non-informative priors $\psi \sim \text{Uniform}(0, 2\Delta)$ and $r \sim \text{Uniform}(0, 1)$. A small value of ψ (close to zero) leads to near independence of the process $Z(\cdot)$, while a large value induces strong spatial dependence; the GMRF approximation is more accurate for smaller values of ψ , and to allow good approximation for large values of ψ , we choose the automatic outer extension distance of the Delaunay triangulation in Section 2.2.1 to be sufficiently large (the triangles in Figure 1 cover a large region outside the observation locations). For the parameter γ involved in (3), we choose $\gamma \sim \text{Uniform}(0, 50)$. Assuming $\beta = 0$, γ influences the spatial extremal dependence strongly, by controlling the degrees of freedom of the Student's t survival function in Theorem 3. Small values of γ induce a strong χ_X , while $\gamma \approx 50$ induces a χ_X approximately zero throughout the nonzero distances, and thus equivalent to the spatial χ -measure of a Gaussian process; the choice of the prior bridges the two scenarios effectively. We find updating the Wendland basis range parameter ϕ to be highly challenging, possibly due to high posterior correlation with other model parameters, and hence, we fix ϕ before implementing the MCMC. For three different choices $\phi = \frac{3}{4}\phi_{\min} + \frac{1}{4}\phi_{\max}$, $\phi = \frac{1}{2}\phi_{\min} + \frac{1}{2}\phi_{\max}$, and $\phi = \frac{1}{4}\phi_{\min} + \frac{3}{4}\phi_{\max}$, we run different MCMC chains. Finally, we choose K and ϕ using deviance information criterion (DIC). We model the mean process $\mu(\cdot)$ as $\mu(\mathbf{s}) = D(\mathbf{s})'\boldsymbol{\theta} + \varepsilon_{\mu}(\mathbf{s})$, where $D(\mathbf{s}) = [1, \text{lon}(\mathbf{s}), \text{lat}(\mathbf{s}), \text{elev}(\mathbf{s})]'$ and $\varepsilon_{\mu}(\mathbf{s}) \stackrel{\text{iid}}{\sim} \text{Normal}(0, \tau_{\mu}^{-1})$. The hyperprior choices

are $\boldsymbol{\theta} \sim \text{Normal}(\mathbf{0}, 100^2 \mathbf{I}_4)$ and $\tau_\mu \sim \text{Gamma}(0.1, 0.1)$. Because our main focus is on inference and not on spatial prediction, spatially independent prior choice for $\mu(\cdot)$ is reasonable. The non-informative prior choice for the spatially-invariant precision parameter τ is $\tau \sim \text{Gamma}(0.1, 0.1)$.

Within the MCMC steps, among the parameters and hyperparameters, we update $\mu(\mathbf{s}_i)$, $\boldsymbol{\theta}$, σ_μ^2 , σ^2 using Gibbs sampling, and ψ , γ , and r using adaptive Metropolis-Hastings algorithm. Among the latent random effects, we update $\boldsymbol{\varepsilon}_t^*, t = 1, \dots, T$ using Gibbs sampling, and we update $R_{k,t}^*, k = 1, \dots, K, t = 1, \dots, T$ using adaptive Metropolis-adjusted Langevin algorithm (MALA). Because of the independence assumption across time in (11), we update $\boldsymbol{\varepsilon}_t^*$'s and $R_{k,t}^*$'s (separately for each k) in parallel. Sparse SPDE approximation based construction of $Z(\cdot)$ allows fast updating of $\boldsymbol{\varepsilon}_t^*$'s. Further, the low-rank construction of $R(\cdot)$, with compactly supported basis functions, allows fast updating of $R_{k,t}^*$'s. Finally, we impute the censored observations below the thresholds jointly using Gibbs sampling; thanks to the nugget $\boldsymbol{\eta}$ in (8) for allowing fast univariate updating. The full conditional distributions are in the Supplementary Material.

We implement the MCMC algorithm in R (<http://www.r-project.org>). For the data application, we generate 100,000 posterior samples and discard the first 50,000 iterations as burn-in period. Subsequently, we thin the Markov chains by keeping one out of five consecutive samples and thus, we finally obtain 10,000 samples for drawing posterior inference. Due to high computational burden, we consider the burn-in and post-burn-in lengths of the MCMC chains to be 50,000 and 25,000, respectively, and the same thinning, for the simulation studies. Convergence and mixing are monitored through trace plots.

4 Simulation Studies

In this section, we demonstrate the performance of the proposed model and the related Bayesian computational technique in terms of the convergence of the MCMC chains to the true parameter values and coverage probabilities of the true pairwise χ -measure. For the study

design, we stick to the spatial domain and time points being same as that for the data application; we simulate datasets at 195 grid cells over Bangladesh at a resolution of $0.25^\circ \times 0.25^\circ$ for 2440 temporal replications, using (11), for each $K = 3^2, 4^2, 5^2, 6^2$. The true parameter choices are $\mu(\mathbf{s}) = 5 + 0.25\text{lon}(\mathbf{s})^2 + 0.25\text{lat}(\mathbf{s})^2 + 0.25\text{elev}(\mathbf{s})^2$, $\tau = 10$, $\psi = 0.15\Delta_{\mathcal{S}} = 0.946$, $r = 0.9$, and $\gamma = 5$. We fix $\phi = \frac{3}{4}\phi_{\min} + \frac{1}{4}\phi_{\max}$ which resembles more accurately with the data application scenario. At each spatial location, we censor the observations below 0.95-th data quantile and impute the censored observations. Some trace plots are presented in Figure 5. After thinning, we show 10,000 MCMC samples where the first 5,000 samples represent the burn-in period. Despite the starting values being significantly different from the true parameter values, all the trace plots converge to the true parameter values. Despite a large number of latent variables requiring Metropolis-Hastings updates and high censoring, the mixing of the MCMC chains is reasonably well. Estimating the shape parameter γ in (3) appears to be the most challenging task and a reasonably large burn-in period is required. We repeated the experiment a large number of times and the convergence of the trace plots is observed for all the instances. Based on 100 simulated datasets, we calculate the average posterior means and average posterior standard deviations for the model parameters and present in Table 1. The average posterior means are close to the true parameter choices and the average posterior standard deviations are small.

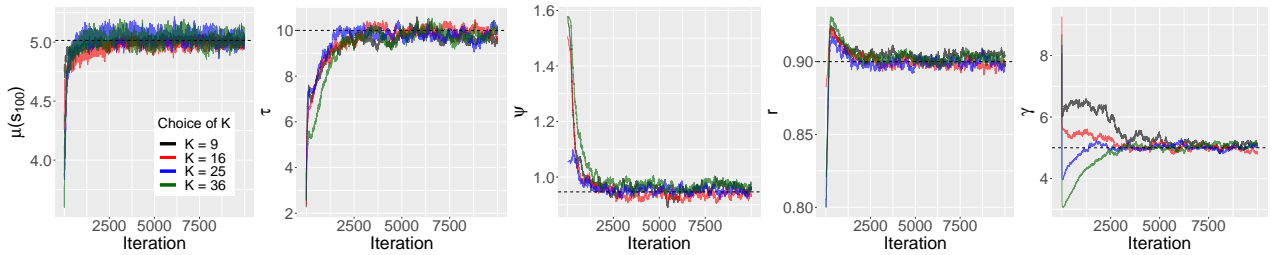


Figure 5: Trace plots (thinned MCMC chains) of some of the model parameters. The corresponding true parameter choices are shown using the dashed horizontal lines.

Based on the true parameter choices, we compute pairwise true χ using (3). Besides, for each of the 5,000 posterior samples, we calculate pairwise χ using (3), and further compute 95% posterior credible intervals. For some pairs of sites allowing small through high values

Table 1: Average posterior means and average posterior standard deviations of the model parameters, based on 100 simulated datasets. The corresponding true values are $\mu(\mathbf{s}_{100}) = 5.014$, $\tau = 10$, $\psi = 0.946$, $r = 0.9$, and $\gamma = 5$.

Choice of K	$\mu(\mathbf{s}_{100})$	τ	ψ	r	γ
$K = 3^2$	5.008 (0.021)	9.678 (0.223)	0.954 (0.013)	0.901 (0.002)	5.075 (0.095)
$K = 4^2$	5.015 (0.029)	9.745 (0.218)	0.953 (0.013)	0.901 (0.002)	5.029 (0.097)
$K = 5^2$	5.034 (0.043)	9.764 (0.218)	0.951 (0.013)	0.901 (0.002)	4.979 (0.100)
$K = 6^2$	5.033 (0.043)	9.737 (0.212)	0.953 (0.013)	0.901 (0.002)	4.993 (0.087)

of true χ , we show the residual χ , that is, the posterior median χ minus true χ and the corresponding 95% posterior credible intervals (adjusted by subtracting true χ), in Figure 6. The credible intervals include zero and they are wider for higher values of true χ . Besides, the credible intervals are wider when considering $K = 9$ basis functions compared to $K = 25$. The credible intervals for highest true χ values span approximately between $(-0.015, 0.02)$ for $K = 9$ and $(-0.01, 0.01)$ for $K = 25$, and this indicates that the estimation error is reasonably small.

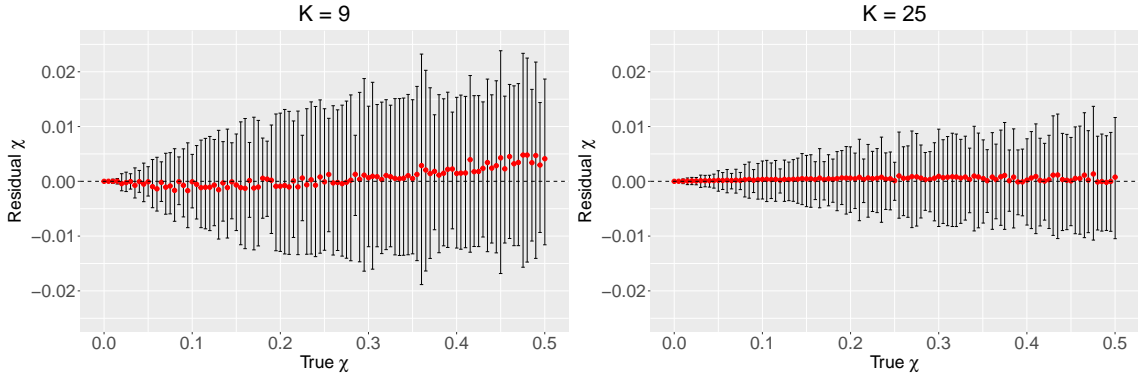


Figure 6: Residual χ (shown using red dots), that is, the posterior median χ minus true χ and the corresponding 95% posterior credible intervals (shown using bars), for some pairs of sites allowing small through high values of true χ .

5 Data application

5.1 The precipitation dataset and exploratory analysis

We consider the daily precipitation data obtained from the project Tropical Rainfall Measuring Mission (TRMM, Version 7, <https://gpm.nasa.gov/data-access/downloads/trmm>) avail-

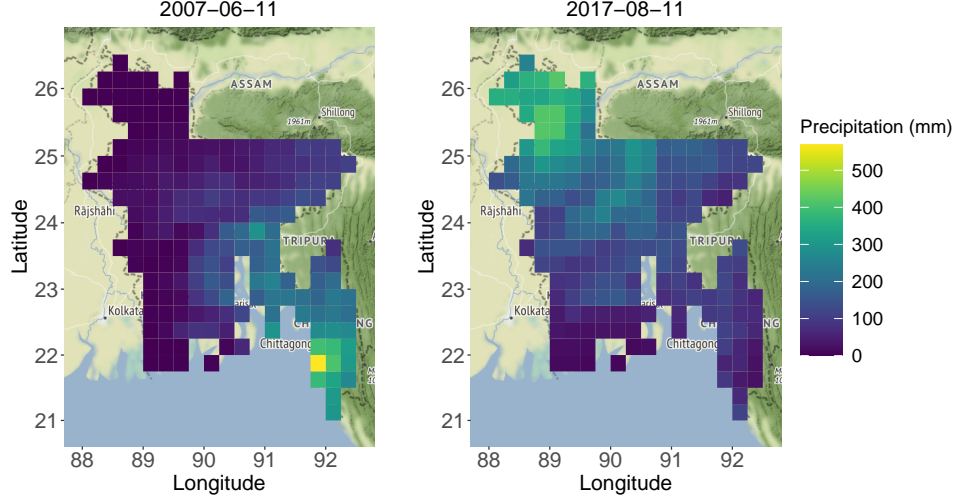


Figure 7: Spatial maps of daily precipitation for the day having largest precipitation at one grid cell (left) and the day with mean spatial precipitation being maximum (right). Both the figures are in same scale.

able over the period March 2000 through December 2019 at a spatial resolution of $0.25^\circ \times 0.25^\circ$; considering the whole Bangladesh, we have data available at 195 grid cells. In order to study heavy rainfall that affects monsoon crops, we consider data only for the months June through September and thus, finally, we have 2440 temporal replications.

The spatial maps of daily precipitation, for the day having largest precipitation at one grid cell (left panel) and the day with mean spatial precipitation being maximum (right panel), are provided in Figure 7. In the left panel, the recorded precipitation is extremely high at one grid cell and a large nearby area faces high through moderate rainfall, whereas the precipitation throughout the western region is practically nil (exactly nil at 39 grid cells). This indicates the local behavior of the shocks that cause extreme precipitation. In the right panel, we observe moderately high values over a large region, but the values decrease gradually with distance from that region. Here all the grid cells receive positive rainfall and hence, a long-range spatial dependence in the moderate rainfall level is likely to be present. Thus, while modeling the extremal dependence, the influence of the moderate rainfall events should be censored.

For exploratory analysis, we consider the 0.95^{th} empirical marginal quantiles as thresholds, and analyze the threshold exceedances. As the clustering of the temporal exceedances

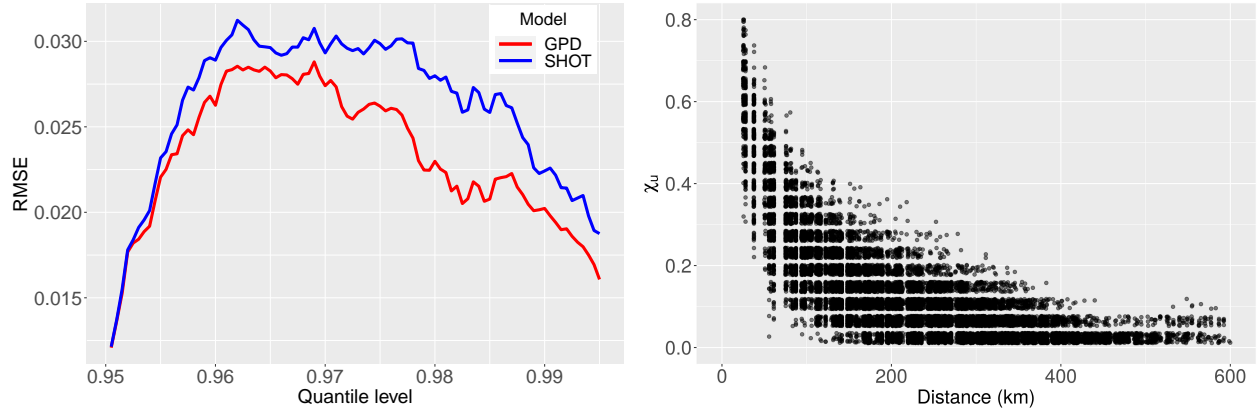


Figure 8: Left: Root mean squared fitting errors (RMSEs) between the quantiles of the uniform transformed exceedances, based on the models GPD and HOT, with the Uniform(0, 1) quantiles. A model with smaller RMSE is preferred. Right: Distances between the pairs of grid cells versus empirical estimates of pairwise χ -measure χ_u for $u = 0.99$.

is possible due to considering daily data, we compute the temporal autocorrelation of the exceedances at lag-1 using Pearson’s correlation, Spearman’s rank correlation, and Kendall’s tau, for testing (separately at each grid cell) the null hypotheses of the lag-1 autocorrelations being zero. We obtain the spatial average p -values for these tests to be 0.490, 0.492, and 0.508, respectively, and hence, we safely ignore temporal dependence. Further, we study the presence of trends in the threshold exceedances at each grid cell, by fitting the generalized Pareto distribution (GPD), the only asymptotically justified model for high threshold exceedances based on EVT, with the logarithm of scale parameters having a linear trend component across years (Coles et al., 2001, Section 6.3.4). For testing the null hypothesis that there is no trend, the spatial average of the site-wise p -values is 0.528 (assuming normality of the estimators), indicating that a stationary assumption across the years is reasonable.

Because we consider only spatially-invariant precision τ in our model, we center and scale the data by subtracting the median of the positive observations at each site followed by dividing the residual by interquartile range (IQR) of the positive observations. As our main goal is in estimating the shape of the tail and the extremal dependence, this preprocessing step is justified. While presenting the final results, we multiply the final residuals by IQR and add the center of the data back. We fit only the data exceeding 0.95-th marginal quantiles

and hence, the center and scale we choose here do not influence the tail directly.

Further, we compare the marginal fits of GPD with that based on the Gaussian scale mixture margins in (11); if the SHOT model in (11) fits the margins equally well or better than GPD, we can avoid a copula-based approach. At a grid cell \mathbf{s}_i , suppose the 0.95th empirical marginal quantile is u_i . For GPD, we fit the threshold exceedances $Y_t(\mathbf{s}_i) \stackrel{\text{iid}}{\sim} \text{GPD}(u_i, \sigma_i, \xi_i)$, where σ_i and ξ_i are the scale and shape parameters. Once the model parameters are estimated (using maximum likelihood estimates, ignoring spatial dependence), we plug them into the CDFs (suppose $\hat{F}_{\text{GPD}}^{(i)}$ and $\hat{F}_{\text{SHOT}}^{(i)}$, respectively) and evaluate the threshold exceedances at those estimated CDFs. In case the models fit the margins well, the exceedances evaluated at the estimated CDFs, that is, $\hat{F}_{\text{GPD}}^{(i)}(Y_t(\mathbf{s}_i))$ and $\hat{F}_{\text{SHOT}}^{(i)}(Y_t(\mathbf{s}_i))$ should be approximately uniformly distributed (call them uniform transformed exceedances), and hence we compare their quantiles with the Uniform(0,1) quantiles. For each quantile level of 0.9505, 0.9510, \dots , 0.9950 of the full data (level of $q = 0.01, 0.02, \dots, 0.9$ of the threshold exceedances, respectively), suppose $U_{\text{GPD}}^{(i,q)}$ and $U_{\text{SHOT}}^{(i,q)}$ denote the q -th quantiles of $\hat{F}_{\text{GPD}}^{(i)}(Y_t(\mathbf{s}_i))$ and $\hat{F}_{\text{SHOT}}^{(i)}(Y_t(\mathbf{s}_i))$, respectively, and we calculate $\text{RMSE}_{\text{GPD}}^{(q)} = \{N^{-1} \sum_{i=1}^N (U_{\text{GPD}}^{(i,q)} - q)^2\}^{1/2}$ and $\text{RMSE}_{\text{SHOT}}^{(q)} = \{N^{-1} \sum_{i=1}^N (U_{\text{SHOT}}^{(i,q)} - q)^2\}^{1/2}$. Here, a model with smaller RMSE is preferred. We present q versus $\text{RMSE}_{\text{GPD}}^{(q)}$ and $\text{RMSE}_{\text{SHOT}}^{(q)}$ in the left panel of Figure 8. Although SHOT has larger RMSE than GPD throughout the high quantiles, the difference is small with the highest difference being 0.0058. Hence, considering the gain in computation and easy interpretation, the unified approach of modeling margins and dependence simultaneously using SHOT is preferred.

For investigating the extremal dependence structure, we compute the χ -measure between all the pairs of grid cells. In the right panel of Figure 8, we present the distances (in kilometers) between the pairs of grid cells along the X-axis, and the empirical estimates of pairwise χ -measure, for $u = 0.99$, along the Y-axis. For large distances, the empirical estimates show evidences of extremal independence while showing strong extremal dependence for small distances; this indicates that a model exhibiting either extremal dependence or extremal

independence throughout Bangladesh is not apt for modeling extreme monsoon rainfall.

5.2 Model comparison

In this section, we compare the proposed model with a GMRF and the single scale mixture process HOT; considering the competing models to be sparse, we also replace the underlying Gaussian process in [Huser et al. \(2017\)](#) by a GMRF. For the proposed model, we choose different alternatives $K = 3^2, 4^2, 5^2, 6^2$ and $\phi = \frac{3}{4}\phi_{\min} + \frac{1}{4}\phi_{\max}, \frac{1}{2}\phi_{\min} + \frac{1}{2}\phi_{\max}, \frac{1}{4}\phi_{\min} + \frac{3}{4}\phi_{\max}$. First, we compare the models based on (scaled) deviance information criterion (DIC); a model with smaller value of DIC is preferred. We divide the final DIC values by 475800, the total number of spatiotemporal observations. For GMRF and HOT, DIC values are -6.560 and -7.644, respectively. The DIC values for different choices of K and ϕ for the SHOT model are presented in Table 2. For $K = 25$ and $\phi = \frac{3}{4}\phi_{\min} + \frac{1}{4}\phi_{\max}$, we observe the smallest value of DIC and use these choices of K and ϕ for drawing inferences. While a large choice of K is expected to approximate the stationary behavior of (9) more accurately as shown in Figure 3, higher number of latent variables lead to less stability. While DIC drops with increasing K for $\phi = \frac{1}{2}\phi_{\min} + \frac{1}{2}\phi_{\max}$, for other choices of ϕ , DIC is smaller for $K = 5^2$ compared to $K = 6^2$.

Table 2: Deviance information criterion (DIC) of the proposed SHOT model for different choices of K and ϕ . A smaller value of DIC is preferred.

Choice of K	$\phi = \frac{3}{4}\phi_{\min} + \frac{1}{4}\phi_{\max}$	$\phi = \frac{1}{2}\phi_{\min} + \frac{1}{2}\phi_{\max}$	$\phi = \frac{1}{4}\phi_{\min} + \frac{3}{4}\phi_{\max}$
$K = 3^2$	-7.583	-7.394	-7.875
$K = 4^2$	-8.098	-8.502	-8.014
$K = 5^2$	-9.276	-8.746	-8.552
$K = 6^2$	-8.710	-8.759	-8.168

The computation times for GMRF, HOT and the four cases $K = 3^2, 4^2, 5^2, 6^2$ (averaged across different choices of ϕ) are 579.44 minutes, 623.94 minutes, 677.72 minutes, 712.29 minutes, 717.51 minutes, and 758.91 minutes, respectively (MCMC chains were run on different nodes of the KAUST IBEX cluster). Despite a large number of additional latent variables that are updated using Metropolis-adjusted Langevin algorithm, the computation time for SHOT model is only 1.24 times (for $K = 5^2$) to that for GMRF.

For the final SHOT model ($K = 5^2$ and $\phi = \frac{3}{4}\phi_{\min} + \frac{1}{4}\phi_{\max}$), the trace plots of some model parameters are presented in Figure 9. All the MCMC chains shows convergence after a certain burn-in period. Similar to the simulated datasets, convergence of the MCMC cgains for the parameter γ appears to be challenging and a reasonably large burn-in period is required. Mixing of the MCMC samples for most of the parameter is reasonably well.

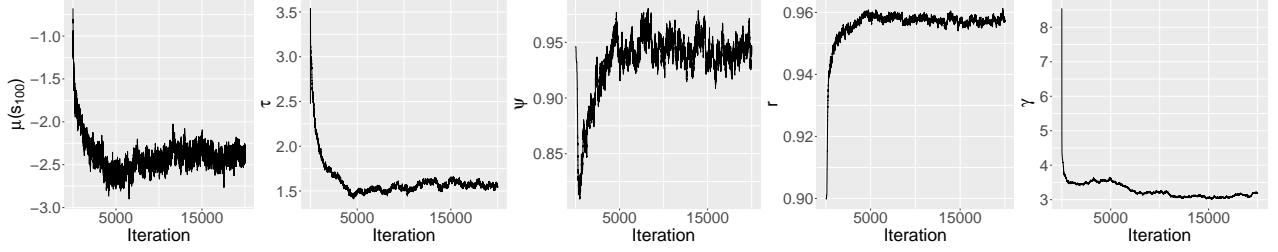


Figure 9: Trace plots (thinned MCMC chains) of some parameters of the SHOT model with $K = 5^2$ and $\phi = \frac{3}{4}\phi_{\min} + \frac{1}{4}\phi_{\max}$. After thinning, burn-in period is the first 10,000 iterations.

In order to compare high marginal data quantiles and the corresponding model quantiles, for each posterior sample from the model parameters, we compute 0.99-th model quantile empirically for all the three models GMRF, HOT, and SHOT, and for a representative pixel at (22.875°N, 91.875°E), some high data quantiles (between quantile levels 0.95 and 0.995) and the corresponding 95% credible regions are presented in the left panel of Figure 10. For lower quantile levels, the posterior medians for all three models are close to the data quantiles. However, for larger quantile levels, the posterior medians are generally higher than the data quantiles. While the credible intervals based on the SHOT model cover the data quantiles for most of the quantile levels, the credible intervals for GMRF and HOT models do not include the data quantiles for a large number of cases. While there is a high uncertainty involved in the high empirical quantile of the data distribution, the proposed approach can provide reasonable credible regions for high quantile levels.

For low through high distances (20km, 40km, ..., and bandwidth of 20km), we present the boxplots of empirical χ_u for $u = 0.99$, calculated using (4), in the right panel of Figure 10. We also empirically calculate $\chi_{0.99}$ for the models GMRF, HOT, and SHOT, and present

in the same figure. For small distances, $\chi_{0.99}$ for HOT and SHOT are close to the median empirical $\chi_{0.99}$, but the estimate based on GMRF is slightly smaller. The $\chi_{0.99}$ estimates based on GMRF are close to the median empirical $\chi_{0.99}$ for moderate through high distances, and the corresponding curve (solid red line) converges to zero as the distance increases. While $\chi_{0.99}$ estimates based on HOT are reasonably close to the median empirical $\chi_{0.99}$ for short distances, the corresponding curve (solid blue line) do not converge towards zero, even if the last few boxplots are concentrated near zero. For the SHOT model, the $\chi_{0.99}$ curve is close to empirical $\chi_{0.99}$ medians for distances smaller than 100km, slightly smaller than empirical $\chi_{0.99}$ for medium distances, and converges to zero for large distances. Similar to the high uncertainty involved in the high empirical marginal quantiles, the empirical estimates of $\chi_{0.99}$ involves high uncertainty in practice. Thus, a limiting choice (model chosen based on χ , but not based on χ_u for $u < 1$) is preferred; the theoretical values of χ for the three models are presented through dashed lines. The theoretical χ for GMRF is always zero which is practically unreliable. For HOT, theoretical χ does not converge to zero as distance increases which is again practically unreliable. Alternatively, the theoretical χ profile for the SHOT model is positive at short distances and converges to zero for large distances; this is a more practically justified scenario and hence, SHOT is preferred than others. For sub-asymptotic level $u = 0.99$, due to high uncertainty involved in the estimates, preferring a model than others is difficult and thus, a model with smaller DIC should be preferred.

5.3 Inference

Here we discuss two types of tail-inference: first, the marginal inference, and second, the tail-properties of the spatial aggregates. For marginal inferences, we obtain spatial return level maps of one-year, five-year, and ten-year return levels. Because we have only data for 122 days during June through September every year, m -th year return level is the $(1 - 1/122m)$ -th quantile of the marginal distribution. Because of the non-existence of the closed form expression of the marginal distributions for the model (11), return levels are calculated

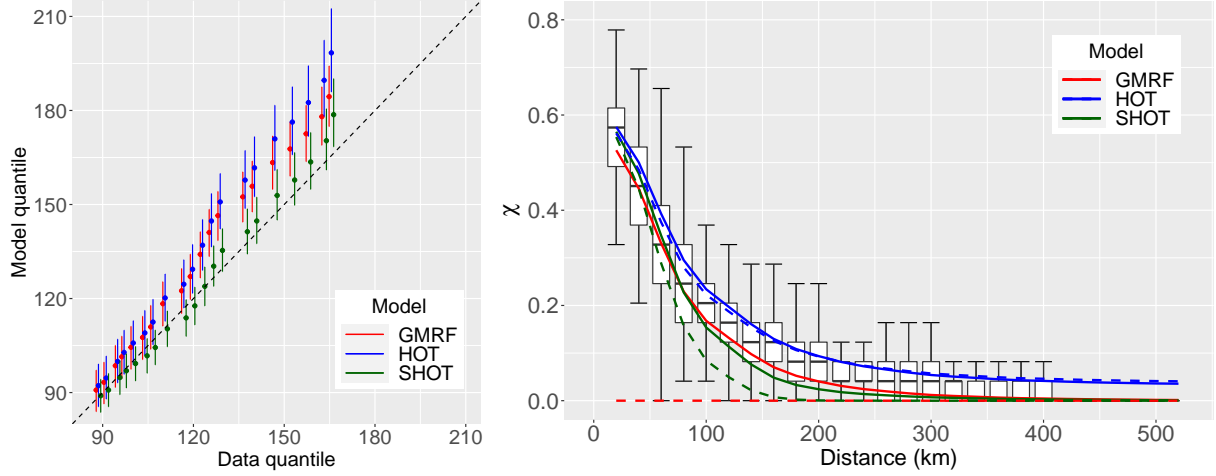


Figure 10: Left: Data quantiles versus model-based marginal quantiles for levels between 0.95 and 0.995, at a representative pixel at (22.875°N, 91.875°E). The dots represent the corresponding posterior medians and the bars represent the corresponding 95% credible regions. Right: Boxplots of empirical χ_u for $u = 0.99$, calculated using (4), for low through high distances (20km, 40km, ..., and bandwidth of 20km). The overlapped solid lines represent the fitted $\chi_{0.99}$ curve based on different models and the dashed lines represent the theoretical χ as a function of distance.

empirically for each posterior sample from the parameter space. Further, we obtain the posterior mean and standard deviation at every pixel based on the MCMC samples of the empirical return levels and present them in Figure 11. The posterior means of one-year return levels vary between 95.09mm and 235.73mm, where the smallest values are observed near the southwestern region and the highest values are observed near the Himalayan foothills of the northeastern region. The posterior means of the five-year return levels vary between 146.13mm and 354.32mm while that for the ten-year return levels vary between 175.11mm and 423.62mm; the spatial patterns are similar for all the three cases. The posterior standard deviations exhibit similar spatial pattern to that of posterior means and they are larger for the ten-year return levels compared to that of one-year and five-year return levels. The non-smooth behavior of the spatial maps is observed for several instances in Figure 11 which is also visible in the pixel-wise medians and the inter-quartile ranges of the TRMM dataset and not necessarily due to the non-smooth surfaces simulated from model (11).

Further, we draw inference about the spatial aggregates, where we divide Bangladesh into

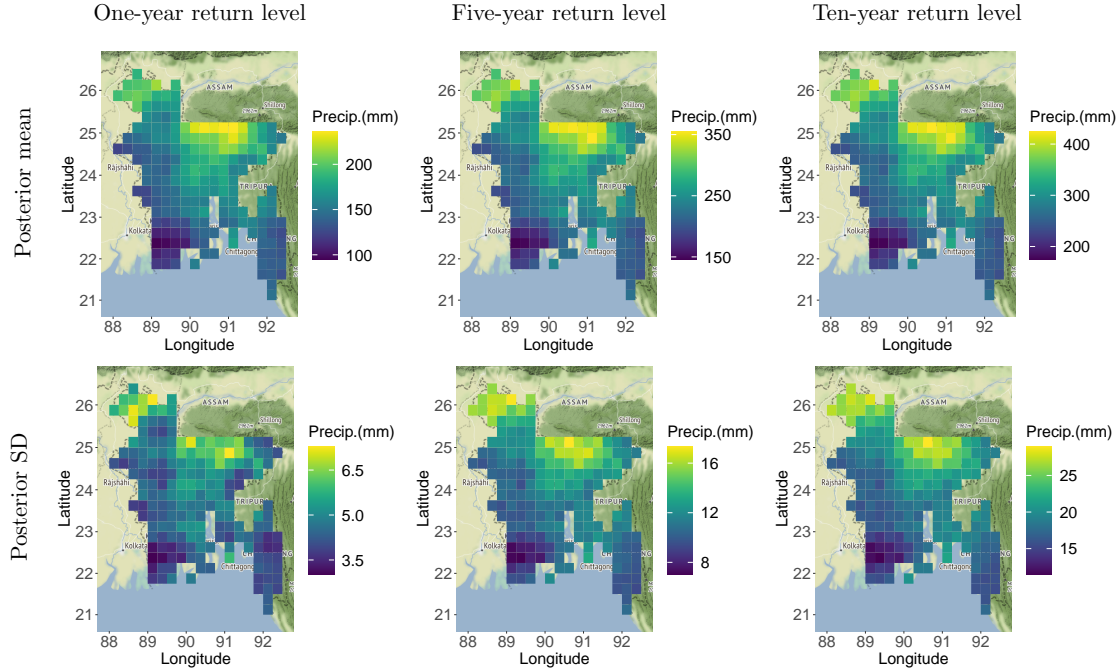


Figure 11: Spatial maps of posterior means and standard deviations of one-year, five-year, and ten-year return levels.

six regions according to the definition used by [Mannan and Karmakar \(2007\)](#) in the context of heavy rainfall analysis in Bangladesh. Instead of treating the return levels of the sum of the precipitation amounts across the pixels within a region, we present the posterior mean and standard deviations of the spatial averages (representative of rainfall within a pixel of dimension $0.25^\circ \times 0.25^\circ$) in Table 3. The posterior mean is the highest for the North-East region while it is the smallest for the South-West region for all the return periods, and this pattern is consistent with the spatial maps presented in Figure 11. The posterior standard deviations for the one-year return levels are close to 3, while they are approximately near 7 for the five-year return levels and are approximately near 11 for the ten-year return levels. The approximately similar values of the posterior standard deviations across the regions is consistent with Theorem 1.

Table 3: Posterior means and standard deviations (within brackets) of one-year, five-year, and ten-year return levels of the spatial average precipitation at six geographical regions of Bangladesh (in mm).

Region	One-year return level	Five-year return level	Ten-year return level
North-West	110.191 (3.133)	162.668 (6.924)	189.567 (10.864)
North-East	141.571 (3.568)	202.990 (8.102)	234.532 (12.729)
West-Central	110.898 (3.376)	167.296 (7.340)	196.149 (11.597)
East-Central	117.145 (3.185)	168.922 (6.835)	195.148 (10.614)
South-West	89.139 (2.951)	133.973 (6.015)	156.964 (9.317)
South-East	103.785 (2.761)	149.874 (6.174)	174.056 (9.845)

6 Discussions and Conclusions

6.1 Summary

We propose a novel hierarchical Bayesian model that allows short-range extremal dependence and long-range independence. Most of the existing approaches for modeling spatial extremes using Gaussian location and/or scale mixture models are tenable for small geographical domains as they allow extremal dependence between all pairs of sites, which is practically unrealistic for most natural processes like precipitation fields. The other existing models consider spatial random partitioning to alleviate long-range extremal dependence; however, they are computationally challenging due to the imputation of the partition indexes and the long-range extremal independence is not theoretically satisfied unless an infinite partitioning of the spatial domain is considered. The proposed model in this paper allows a closed-form expression of the spatial extremal dependence measure and we discuss construction of the stochastic process in such a way (using Wendland basis functions) that the spatial range of the extremal dependence can be controlled using a model parameter. The construction of the underlying Gaussian process is done using stochastic partial differential equation that allows sparse precision matrices leading to faster computation. The Bayesian inferential procedure is a combination of Gibbs sampling, adaptive random walk Metropolis-Hastings algorithm and adaptive Metropolis-adjusted Langevin algorithm.

6.2 Drawbacks

The model assumes that the observations are independent across time which can be a restrictive assumption in some applications. In case of temporal extremal dependence, the random scale terms would be dependent across time and hence, they cannot be updated in parallel. For a large number of temporal replications, the imputation can be computationally intensive. We find that updating the Wendland basis range parameter ϕ within MCMC is challenging, due to strong posterior correlation between the model parameters. In the implementation of the model, we thus choose ϕ based on crossvalidation. Besides, the parameters τ and γ has high posterior correlation; large values of τ and γ both indicate smaller variance. However, convergence is poor while updating them simultaneously within MCMC; a different parametrization could be a possible solution. While drawing inferences, we need to calculate the marginal high quantiles empirically for each posterior sample from the parameter space due to the non-existence of the closed form expression of the marginal distributions.

6.3 Other Applications

While we illustrate the proposed model for precipitation data, this can be used for other types of variables like ozone or $\text{PM}_{2.5}$ concentration as well. While we fit the model only to the threshold exceedances, the same model could be used for drawing inferences about the bulk properties. In this paper, we concentrated on model fitting and drawing inferences rather than predicting the high quantiles at an unobserved site. A similar model can be used for that purpose; the prior of the mean process $\mu(\cdot)$ assumes independence across space here, but in case the spatial prediction is the main goal, a spatially dependent prior should be chosen.

6.4 Possible Extensions

In case of temporal extremal dependence, the temporal partitioning approach of [Krupskii and Genton \(2017\)](#) can be incorporated along with modeling the spatial dependence as described here. Instead of relying on a parametric model and censoring the observations below certain

high thresholds, a semiparametric model can be considered following [Hazra et al. \(2018\)](#) and [Hazra and Huser \(2021\)](#). To bypass computational burden, we consider a sparse Gaussian process here. However, several approaches for handling high-dimensional spatial datasets have been proposed in the literature; [Heaton et al. \(2019\)](#) summarize a list of such approaches and they can be used possible alternatives for constructing the underlying Gaussian process.

References

- Bakka, H., Rue, H., Fuglstad, G.-A., Riebler, A., Bolin, D., Illian, J., Krainski, E., Simpson, D., and Lindgren, F. (2018). Spatial modeling with R-INLA: A review. *Wiley Interdisciplinary Reviews: Computational Statistics*, 10(6):e1443.
- Breiman, L. (1965). On some limit theorems similar to the arc-sin law. *Theory of Probability & Its Applications*, 10(2):323–331.
- Brown, B. M. and Resnick, S. I. (1977). Extreme values of independent stochastic processes. *Journal of Applied Probability*, 14(4):732–739.
- Busby, J. W., Baker, K., Bazilian, M. D., Gilbert, A. Q., Grubert, E., Rai, V., Rhodes, J. D., Shidore, S., Smith, C. A., and Webber, M. E. (2021). Cascading risks: Understanding the 2021 winter blackout in Texas. *Energy Research & Social Science*, 77:102106.
- Calliari, E., Mysiak, J., and Vanhala, L. (2020). A digital climate summit to maintain paris agreement ambition. *Nature Climate Change*, 10(6):480–480.
- Chen, Y., Moufouma-Okia, W., Masson-Delmotte, V., Zhai, P., and Pirani, A. (2018). Recent progress and emerging topics on weather and climate extremes since the fifth assessment report of the intergovernmental panel on climate change. *Annual Review of Environment and Resources*, 43:35–59.
- Ciarlet, P. G. (2002). *The finite element method for elliptic problems*. SIAM.

- Coles, S., Bawa, J., Trenner, L., and Dorazio, P. (2001). *An introduction to statistical modeling of extreme values*, volume 208. Springer.
- Coles, S., Heffernan, J., and Tawn, J. (1999). Dependence measures for extreme value analyses. *Extremes*, 2(4):339–365.
- Davison, A. C., Huser, R., and Thibaud, E. (2019). Spatial Extremes. In Gelfand, A. E., Fuentes, M., Hoeting, J. A., and Smith, R. L., editors, *Handbook of Environmental and Ecological Statistics*, pages 711–744. CRC Press.
- Davison, A. C., Padoan, S. A., and Ribatet, M. (2012). Statistical modeling of spatial extremes. *Statistical Science*, 27(2):161–186.
- de Fondeville, R. and Davison, A. C. (2018). High-dimensional peaks-over-threshold inference. *Biometrika*, 105(3):575–592.
- Dombry, C. and Ribatet, M. (2015). Functional regular variations, Pareto processes and peaks over threshold. *Statistics and its Interface*, 8(1):9–17.
- Engelke, S. and Hitz, A. S. (2020). Graphical models for extremes. *Journal of the Royal Statistical Society: Series B (Statistical Methodology)*, 82(4):871–932.
- Ghosh, S., Das, D., Kao, S.-C., and Ganguly, A. R. (2012). Lack of uniform trends but increasing spatial variability in observed indian rainfall extremes. *Nature Climate Change*, 2(2):86–91.
- Green, P. J. and Sibson, R. (1978). Computing Dirichlet tessellations in the plane. *The computer journal*, 21(2):168–173.
- Guinness, J. (2018). Permutation and grouping methods for sharpening gaussian process approximations. *Technometrics*, 60(4):415–429.

- Hazra, A. and Huser, R. (2021). Estimating high-resolution Red Sea surface temperature hotspots, using a low-rank semiparametric spatial model. *The Annals of Applied Statistics*, 15(2):572 – 596.
- Hazra, A., Reich, B. J., Shaby, B. A., and Staicu, A.-M. (2018). A semiparametric Bayesian model for spatiotemporal extremes. *arXiv preprint arXiv:1812.11699*.
- Hazra, A., Reich, B. J., and Staicu, A.-M. (2020). A multivariate spatial skew-t process for joint modeling of extreme precipitation indexes. *Environmetrics*, 31(3):e2602.
- Heaton, M. J., Datta, A., Finley, A. O., Furrer, R., Guinness, J., Guhaniyogi, R., Gerber, F., Gramacy, R. B., Hammerling, D., Katzfuss, M., et al. (2019). A case study competition among methods for analyzing large spatial data. *Journal of Agricultural, Biological and Environmental Statistics*, 24(3):398–425.
- Huser, R., Opitz, T., and Thibaud, E. (2017). Bridging asymptotic independence and dependence in spatial extremes using Gaussian scale mixtures. *Spatial Statistics*, 21:166–186.
- Huser, R. and Wadsworth, J. L. (2020). Advances in statistical modeling of spatial extremes. *Wiley Interdisciplinary Reviews: Computational Statistics*, page e1537.
- Kabluchko, Z., Schlather, M., and De Haan, L. (2009). Stationary max-stable fields associated to negative definite functions. *The Annals of Probability*, 37(5):2042–2065.
- Kao, S.-C. and Ganguly, A. R. (2011). Intensity, duration, and frequency of precipitation extremes under 21st-century warming scenarios. *Journal of Geophysical Research: Atmospheres*, 116(D16).
- Kharin, V. V., Zwiers, F. W., Zhang, X., and Hegerl, G. C. (2007). Changes in temperature and precipitation extremes in the IPCC ensemble of global coupled model simulations. *Journal of Climate*, 20(8):1419–1444.

- Kim, H.-M., Mallick, B. K., and Holmes, C. (2005). Analyzing nonstationary spatial data using piecewise Gaussian processes. *Journal of the American Statistical Association*, 100(470):653–668.
- Krupskii, P. and Genton, M. G. (2017). Factor copula models for data with spatio-temporal dependence. *Spatial Statistics*, 22:180–195.
- Krupskii, P., Huser, R., and Genton, M. G. (2018). Factor copula models for replicated spatial data. *Journal of the American Statistical Association*, 113(521):467–479.
- Lindgren, F., Bolin, D., and Rue, H. (2021). The SPDE approach for Gaussian and non-Gaussian fields: 10 years and still running. arXiv preprint 2111.01084.
- Lindgren, F. and Rue, H. (2015). Bayesian spatial modelling with R-INLA. *Journal of Statistical Software*, 63:1–25.
- Lindgren, F., Rue, H., and Lindström, J. (2011). An explicit link between gaussian fields and gaussian markov random fields: the stochastic partial differential equation approach. *Journal of the Royal Statistical Society: Series B (Statistical Methodology)*, 73(4):423–498.
- Mannan, M. A. and Karmakar, S. (2007). Climatic features of heavy rainfall activities in monsoon season and its socio-economic impact in Bangladesh. In *Proceedings of SAARC Seminar on Application of Weather and Climate Forecasts in the Socio-economic Development and Disaster Mitigation*, pages 5–7.
- Masson-Delmotte, V., Zhai, P., Priani, A., Connors, S., Péan, C., Berger, S., et al. (2021). Ipcc, 2021: Climate change 2021: The physical science basis. Contribution of Working Group I to the sixth assessment report of the Intergovernmental Panel on Climate Change.
- Morris, S. A., Reich, B. J., Thibaud, E., and Cooley, D. (2017). A space-time skew- t model for threshold exceedances. *Biometrics*, 73(3):749–758.

- Opitz, T. (2013). Extremal t -processes: Elliptical domain of attraction and a spectral representation. *Journal of Multivariate Analysis*, 122:409–413.
- Padoan, S. A., Ribatet, M., and Sisson, S. A. (2010). Likelihood-based inference for max-stable processes. *Journal of the American Statistical Association*, 105(489):263–277.
- Reich, B. J. and Shaby, B. A. (2012). A hierarchical max-stable spatial model for extreme precipitation. *The Annals of Applied Statistics*, 6(4):1430.
- Rue, H. and Held, L. (2005). *Gaussian Markov random fields: theory and applications*. Chapman and Hall/CRC.
- Schlather, M. (2002). Models for stationary max-stable random fields. *Extremes*, 5(1):33–44.
- Shukla, P., Skea, J., Calvo Buendia, E., Masson-Delmotte, V., Pörtner, H., Roberts, D., Zhai, P., Slade, R., Connors, S., Van Diemen, R., et al. (2019). Ipcc, 2019: Climate change and land: an IPCC special report on climate change, desertification, land degradation, sustainable land management, food security, and greenhouse gas fluxes in terrestrial ecosystems.
- Sibuya, M. (1960). Bivariate extreme statistics, i. *Annals of the Institute of Statistical Mathematics*, 11(3):195–210.
- Simpson, E. S., Opitz, T., and Wadsworth, J. L. (2020). High-dimensional modeling of spatial and spatio-temporal conditional extremes using inla and the spde approach. *arXiv preprint arXiv:2011.04486*.
- Smith, R. L. (1990). Max-stable processes and spatial extremes. *Unpublished manuscript*.
- Stott, P. A., Stone, D. A., and Allen, M. R. (2004). Human contribution to the European heatwave of 2003. *Nature*, 432(7017):610–614.
- Thibaud, E. and Opitz, T. (2015). Efficient inference and simulation for elliptical Pareto processes. *Biometrika*, 102(4):855–870.

- Van Oldenborgh, G. J., Van Der Wiel, K., Sebastian, A., Singh, R., Arrighi, J., Otto, F., Haustein, K., Li, S., Vecchi, G., and Cullen, H. (2017). Attribution of extreme rainfall from Hurricane Harvey, August 2017. *Environmental Research Letters*, 12(12):124009.
- Wadsworth, J. L. and Tawn, J. (2019). Higher-dimensional spatial extremes via single-site conditioning. *arXiv preprint arXiv:1912.06560*.
- Zhong, P., Huser, R., and Opitz, T. (2021). Modeling non-stationary temperature maxima based on extremal dependence changing with event magnitude. *The Annals of Applied Statistics*.